EES Batteries

PAPER

View Article Online
View Journal

Cite this: DOI: 10.1039/d6eb00063k

Ultrafast ion-exchange synthesis of 3D lithiophilic scaffolds for high-capacity anode-less all-solid-state batteries

Jihoon Oh,[a,b] Taegeun Lee,[a,b] Noh Joon Lee,[a,b] Yeeun Sohn,[a,b] Sanghun Park,[a,b] Ji Young Kim,[c] Ki Yoon Bae[c] and Jang Wook Choi *[a,b,d]

Anode-less all-solid-state batteries (ALASSBs) represent a cutting-edge energy storage technology that offers a combination of enhanced safety, superior energy density, and streamlined processability. However, their practical application, particularly in high-capacity systems, is curbed by internal short circuits resulting from the uncontrolled growth of metallic lithium (Li) dendrites. In this study, this problem is addressed by introducing a three-dimensional (3D) lithiophilic scaffold with exceptional Li storage capabilities. The scaffold is constructed by exposing a solution of Ag^+ to Ni metal, which reacts *via* an ultrafast ion-exchange process that requires only 30 seconds. The resulting highly porous Ag–Ni scaffold (p-Ag–Ni) comprises Ag nanofibers with an extensive surface area. The scaffold supports stable Li plating in excess of 35 mAh cm^{-2} without short-circuiting and retains 81% of the original capacity after 100 cycles at room temperature (25 °C) with an areal capacity of 2.9 mAh cm^{-2}. Additionally, it demonstrates excellent performance in a pouch-cell under low stack pressure (3 MPa). These results highlight the potential of rapid ion exchange as a facile and efficient strategy for developing protective layers in high-capacity ALASSBs.

Received 19th March 2026,
Accepted 26th May 2026

DOI: 10.1039/d6eb00063k

rsc.li/EESBatteries

Broader context

Anode-less all-solid-state batteries (ASSBs) mark a fundamental departure from conventional cell architectures. By replacing the anode active material with a bare current collector, this design simultaneously enhances energy density and reduces manufacturing complexity. Despite these advantages, practical deployment remains limited by the persistent challenge of stabilizing lithium plating and stripping at high areal capacities. To address this limitation, we introduce a three-dimensional (3D) lithiophilic scaffold engineered to support high-capacity lithium storage. The scaffold is fabricated through a rapid and scalable process: immersing a metallic substrate in an ionic solution containing a more reductive, lithiophilic metal triggers a spontaneous galvanic displacement reaction that completes in under 30 seconds. This approach yields a highly porous network of interconnected lithiophilic nanofibers with a large electrochemically active surface area. Our findings demonstrate that exploiting redox potential differences between dissimilar metals offers a simple yet effective strategy for constructing robust, high-surface-area scaffolds—providing a viable pathway toward stable cycling at practically relevant capacities in anode-less ASSBs.

Introduction

All-solid-state batteries (ASSBs) represent a paradigm-shifting advancement in energy storage technologies by addressing the long-standing safety limitations inherent in conventional lithium (Li)-ion battery (LIB) systems.[1–4] By replacing volatile, flammable liquid electrolytes—characterized by substantial thermal runaway and safety risks—with intrinsically stable ceramic solid electrolytes (SEs), architectures that demonstrate remarkable potential for safe energy storage solutions may be realized.[5–8] Within the expansive landscape of SE materials, sulfide-based compositions have emerged as particularly promising candidates.[9–11] These materials are distinguished by their high ionic conductivity and superior mechanical integrity, which position them at the forefront of potential commercial implementation.[12–14]

The pursuit of higher energy densities has catalyzed intensive research into next-generation anode materials with the

[a]*School of Chemical and Biological Engineering and Institute of Chemical Process, Seoul National University, Seoul, Republic of Korea.*
E-mail: jangwookchoi@snu.ac.kr
[b]*Hyundai Motor Group-Seoul National University (HMG-SNU) Joint Battery Research Center (JBRC), Seoul National University, Seoul, Republic of Korea*
[c]*Advanced Battery Development Team, Hyundai Motor Company, Hwaseong-si, Republic of Korea*
[d]*Seoul National University Energy Initiative (SNUEI), Seoul National University, Seoul, Republic of Korea*

aim of moving beyond conventional graphite.[15–19] In this regard, silicon (Si)[20–25] and Li metal anodes[26–31] have emerged as promising alternatives. Spearheading innovative anode design, anode-less all-solid-state batteries (ALASSBs) represent substantial progress by offering the prospect of high energy densities and streamlined manufacturing methodologies.[32–35] Despite their potential, ALASSBs are confronted by significant challenges stemming from the absence of a Li-ion hosting material. Their most critical impediment is the uncontrolled evolution of metallic Li dendrites, which pose profound performance and safety risks by potentially triggering internal short circuits, particularly at elevated cell capacities.[36–38] Consequently, the development of sophisticated anode protection strategies capable of precisely regulating Li deposition while preventing dendrite penetration has emerged as a research objective paramount to advancing ALASSB technological maturity.

Current protective layer strategies predominantly leverage lithiophilic metallic constituents to preferentially catalyze particular alloying reactions.[39–41] Meticulous engineering of these interfaces enables researchers to effectively modulate the electrochemical dynamics to substantially lower the nucleation overpotential and facilitate more uniform Li metal deposition.[42–44] Although these approaches involving the use of a lithiophilic protective layer have notably improved the performance of ALASSBs, the inherently limited Li storage capabilities of these layers have proved to be a limiting factor by circumscribing their long-term electrochemical efficacy under high-capacity conditions. Paradoxically, these sophisticated manufacturing methodologies compromise the primary technological advantage of ALASSBs: their potential to simplify and streamline manufacturing processes.

To circumvent the existing limitations associated with the ALASSB protective layer, we developed an ultrafast method to synthesize a three-dimensional (3D) lithiophilic porous scaffold by exploiting a straightforward ion-exchange mechanism. Specifically, the immersion of a nickel (Ni) substrate (−0.25 V *vs.* SHE) in a solution enriched with silver (Ag) ions (0.8 V *vs.* SHE) initiates a spontaneous ion-exchange reaction, driven by the inherent differences in the reduction potentials of the two metals. This gives rise to the precipitation of Ag metal on the Ni layer, which generates a unique morphological architecture characterized by Ag nanofibers with an exceptionally large surface area and highly interconnected porosity. The resulting structure demonstrates superior Li storage capabilities.

The synthesis protocol offers advantages from the processing viewpoint, as the 3D scaffold can be produced within 30 seconds. The resulting porous silver–nickel structure (p-Ag–Ni) delivered extraordinary electrochemical performance by enabling Li storage beyond 35 mAh cm^{-2} without short-circuiting. Remarkably, the scaffold maintained robust performance even under low stack pressures of 3 MPa in an ALASSB pouch-cell configuration. This protective layer strategy, based on a highly porous lithiophilic scaffold synthesized using a facile ion-exchange method, represents a significant advancement by simultaneously addressing the critical challenges faced by ALASSBs: the need for high-capacity energy storage and fabrication simplification.

Results and discussion

Among the lithiophilic metals, Ag is considered a promising material for anode-less protective layers, owing to its exceptional lithiophilicity and broad Li solubility range.[45–49] ALASSBs incorporating Ag have been explored extensively by employing advanced configurations such as carbon composites[50] and dual-seed structures with zinc oxide (ZnO).[51] However, these designs are typically disadvantaged by their limited Li storage capacity and constrained surface areas, which lead to Li nucleation and growth either above or beneath the protective layer.

In view of these shortcomings, and to develop high-capacity ALASSBs while mitigating the risk of short-circuiting, the integration of a 3D scaffold seems crucial. Such a scaffold would increase the storage capacity by expanding the spatial volume, and it would enlarge the surface area, which would support efficient Li plating and stripping processes under high-capacity conditions. However, conventional methods for fabricating 3D scaffolds rely on complex and time-consuming techniques such as electrospinning.[52,53] For large-scale production, compatibility with roll-to-roll continuous manufacturing—as employed in conventional LIB production—necessitates a fabrication process that is both rapid and efficient, motivating the development of an improved fabrication strategy. To overcome this limitation, we devised a simple and efficient ion-exchange process to synthesize 3D lithiophilic scaffolds with a large surface area. Particularly, a robust scaffold comprising Ag nanofibers was created by immersing a Ni layer in an aqueous solution of silver nitrate ($AgNO_3$) for only 30 seconds, (Fig. 1a). In ion-exchange–driven metal deposition, a sufficiently high concentration of the metal-ion solution accelerates the reaction kinetics, promoting dendritic growth with a large surface area.[54] To leverage this effect, a relatively high concentration (1 M) of $AgNO_3$ was employed in this study. This scaffold, characterized by its exceptionally large surface area and intrinsic void space, provides ample capacity to accommodate substantial Li deposition, the primary requirement for high-capacity ALASSBs (Fig. 1b).

The p-Ag–Ni layer had a distinctive silver color as a clear visual confirmation of the deposition of Ag metal, thus effectively differentiating it from the original Ni layer prior to the ion-exchange process (Fig. S1, SI). Scanning electron microscopy (SEM) images of the fabricated p-Ag–Ni scaffold revealed the growth of Ag metal into irregularly arranged nanofibers, resulting in a highly porous structure with a substantial surface area (Fig. 2a). A higher resolution image enabled the average thickness of the Ag nanofibers to be determined as 300 nm (Fig. 2b). Energy-dispersive X-ray spectroscopy (EDS) mapping further verified that these nanofibers are composed of Ag metal (Fig. S2, SI). A cross-sectional SEM image of the p-Ag–Ni layer revealed its 3D scaffold structure (Fig. 2c) with a

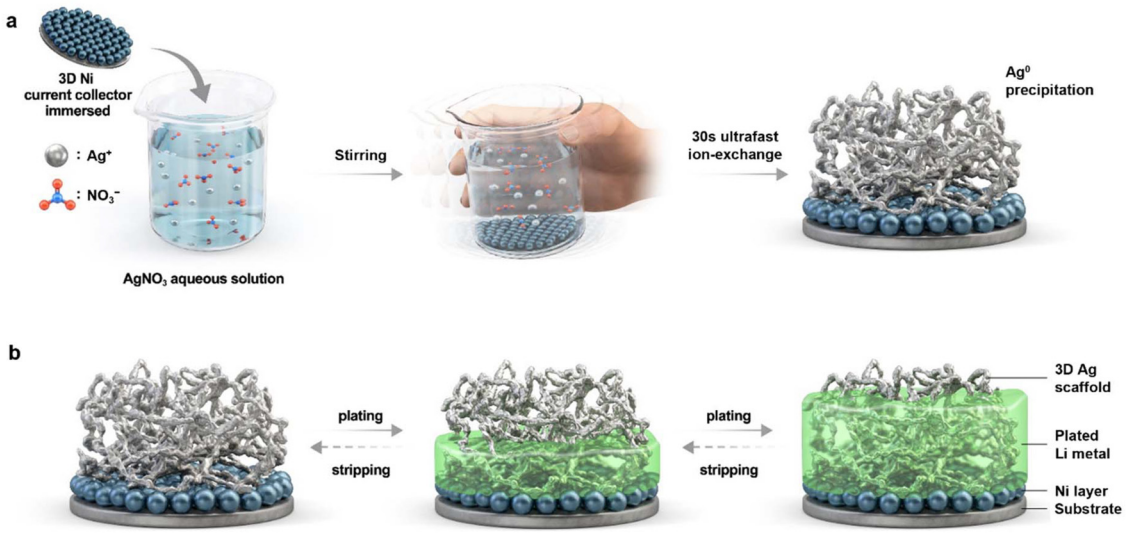

Fig. 1 Schematic illustration of (a) ultrafast ion-exchange synthesis of p-Ag–Ni and (b) Li storage mechanism of p-Ag–Ni during charging.

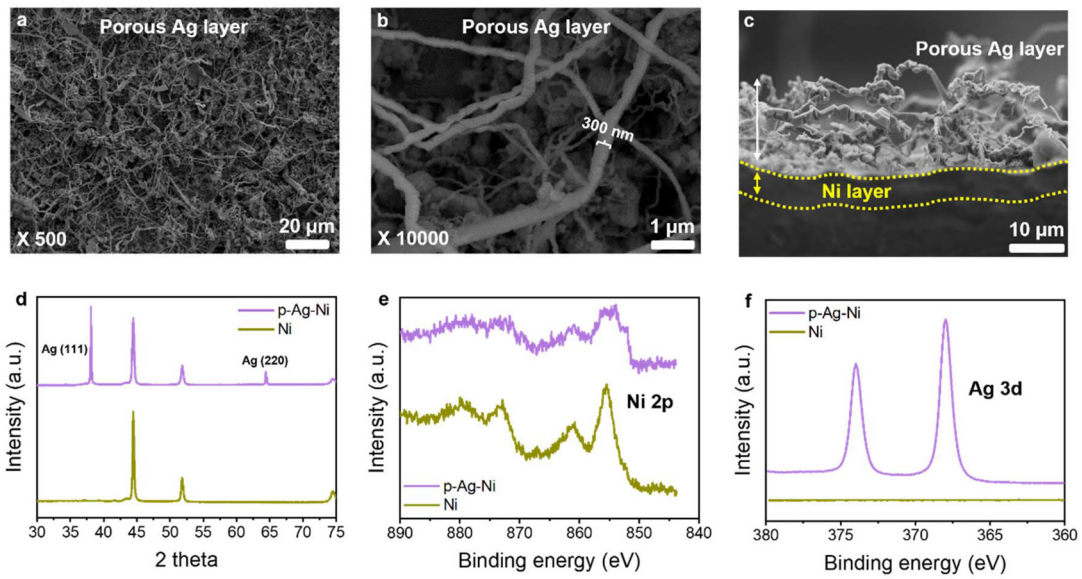

Fig. 2 (a–c) Top-view and cross-sectional SEM images of the p-Ag–Ni layer. (d) XRD patterns comparing p-Ag–Ni and bare Ni electrodes. (e and f) XPS results of the (e) Ni 2p and (f) Ag 3d regions.

total thickness of approximately 20 μm and predominantly consisting of void spaces. This structural design is conducive to stably accommodating a significant amount of Li.

X-ray diffraction (XRD) analysis confirmed the crystalline nature of the scaffold, showing dominant Ag (111) and (220) facets (Fig. 2d). Additionally, X-ray photoelectron spectroscopy (XPS) analysis revealed a reduction in the intensity of Ni 2p peaks and the emergence of prominent Ag 3d peaks, further confirming the successful precipitation of Ag through the ion-exchange process (Fig. 2e and f).

The propensity of the scaffold to support stable Li deposition was investigated by analyzing the charged p-Ag–Ni layer (following Li plating) using cross-sectional SEM-EDS (Fig. 3a). A half-cell configuration was assembled by using a sulfide SE layer comprising Li_6PS_5Cl (LPSCl) on top of the p-Ag–Ni anode-less layer as the working electrode and Li metal as the counter electrode. Then, Li was deposited onto the anode-less layer at a current density of 1 mA cm^{-2} for 3.5 hours, which corresponds to a capacity of 3.5 mAh cm^{-2}. Subsequently, a cross section of the anode-less-layer was inspected after disassembling the cell. The results revealed that Li was stably deposited starting from the base of the p-Ag–Ni scaffold, with the porous Ag layer remaining structurally intact. Notably, the upper portions of the porous Ag scaffold were still unoccupied,

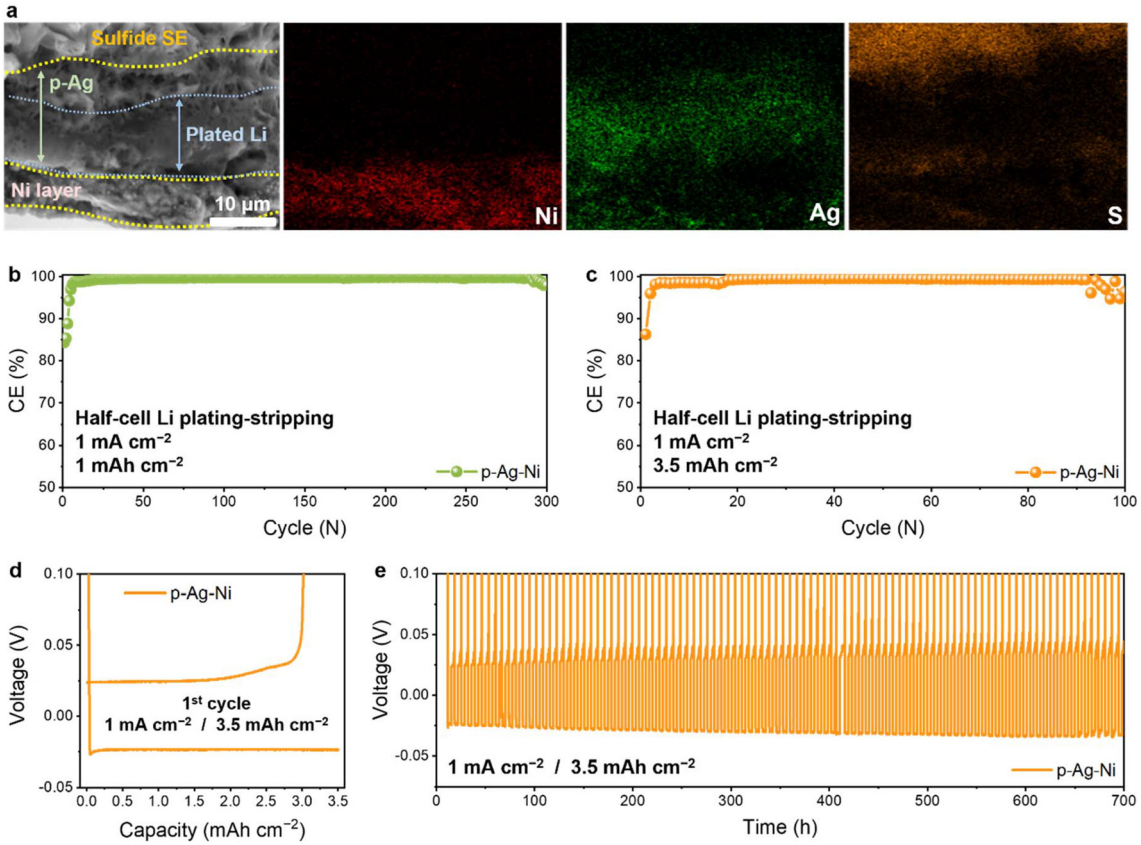

Fig. 3 (a) Cross-sectional SEM images of the p-Ag–Ni layer after the first Li plating (3.5 mAh cm^{-2}). (b–e) Half-cell Li plating-stripping performance at a current density of 1 mA cm^{-2}: coulombic efficiencies (CEs) for capacities of (b) 1.0 mAh cm^{-2} and (c) 3.5 mAh cm^{-2}. (d) First-cycle voltage profile and (e) voltage–time curve for a capacity of 3.5 mAh cm^{-2}.

indicating that the scaffold had additional capacity available to accommodate even larger volumes of Li. This observation underscores the potential of the p-Ag–Ni layer as a robust anode-less protective layer capable of supporting high-capacity Li deposition.

To optimize the concentration of the $AgNO_3$ solution for the ion-exchange process, two concentrations—1 M and 0.5 M—were compared (Fig. S3, SI) by preparing p-Ag–Ni layers under identical reaction conditions with a reaction time of 30 seconds. Thereafter, the cycling stability and coulombic efficiency (CE) of the half-cell were evaluated during repeated Li plating and stripping. The results demonstrated that the 0.5 M solution condition was more susceptible to earlier internal short circuits compared to the 1 M solution. This finding indicates that the concentration of the $AgNO_3$ solution directly influences the extent of Ag scaffold formation during the reaction, as well as the capacity of the scaffold to stably accommodate Li during cycling.

The p-Ag–Ni layer synthesized using the optimized 1 M $AgNO_3$ solution was further evaluated by conducting half-cell plating-stripping tests at three different capacity levels: 0.5 mAh cm^{-2} (Fig. S4, SI), 1 mAh cm^{-2} (Fig. 3b), and 3.5 mAh cm^{-2} (Fig. 3c). Under these conditions, the p-Ag–Ni scaffold cycled stably for 550, 300, and 100 cycles, respectively, confirming its effectiveness as a robust anode-less protective layer. At 3.5 mAh cm^{-2}, the initial coulombic efficiency (ICE) was 86.3% (Fig. 3d), with the system operating successfully for 700 hours without any signs of internal short circuits or significant increases in the overpotential, as evidenced by the voltage–time profile (Fig. 3e). At an even higher capacity of 5 mAh cm^{-2} (Fig. S5, SI), half-cell analysis revealed an ICE of 89.4% and stable cycling performance for 30 cycles, demonstrating the capacity of the p-Ag–Ni scaffold to accommodate Li deposition for extended periods of time.

To benchmark p-Ag–Ni against conventional Ag nanosystems (nanowires and nanoparticles), we evaluated slurry-cast Ag nanowires and Ag nanoparticles. Mg—which, like Ag, forms a solid solution with Li—was also compared. However, due to its high oxidation tendency, an ion-exchanged Mg scaffold was infeasible, and commercial Mg nanowires are not usually available; thus, only Mg nanoparticles were tested. All alternative systems showed lower CEs and premature internal short-circuiting relative to p-Ag–Ni (Fig. S6, SI), indicating that the high surface area and well-defined porosity of the p-Ag–Ni framework enable more stable Li accommodation.

Electrochemical impedance spectroscopy (EIS) measurements were conducted during extended cycling involving repeated Li plating and stripping, with data collected every 10

cycles to monitor variations in the resistance (Fig. S7, SI). The Nyquist profiles plotted throughout the cycling process were consistent, without any significant reduction in the resistance, indicating stable cycling behavior without any sign of internal short circuits. Additionally, the observed increase in resistance during cycling was minimal, demonstrating the high stability of the internal cell configuration even during long-term repeated Li plating and stripping. This stability underscores the robustness of the p-Ag–Ni scaffold and its ability to maintain both interfacial and structural integrity during extended cycling.

The extent to which the p-Ag–Ni scaffold could accommodate extensive Li deposits without short-circuiting was probed by conducting chronopotentiometry analyses in a half-cell configuration. This enabled an extremely high capacity of Li to be continuously deposited onto the anode-less protective layer (Fig. 4a). During the analysis, *in situ* EIS measurements were recorded at regular intervals to sensitively detect any signs of internal short-circuit behavior. Li was deposited at a constant current density of 1 mA cm^{-2}, while EIS measurements were taken every hour, corresponding to a capacity increment of 1 mAh cm^{-2}. The Nyquist plots from the *in situ* EIS analysis showed that the resistance level was consistently maintained as Li deposition progressed (Fig. 4b). This trend was observed even at higher capacities of 30 mAh cm^{-2} and 40 mAh cm^{-2} (Fig. S8, SI). Internal short circuits typically lower the resistance dramatically due to significant electronic conduction,[55] but the absence of such a decrease in resistance confirmed that internal short circuits did not occur during Li deposition.

Further analysis using an equivalent circuit model (insets in Fig. 4c and d) corroborated these findings. The bulk resistance (R_b), corresponding to the *x*-axis intercept of the Nyquist

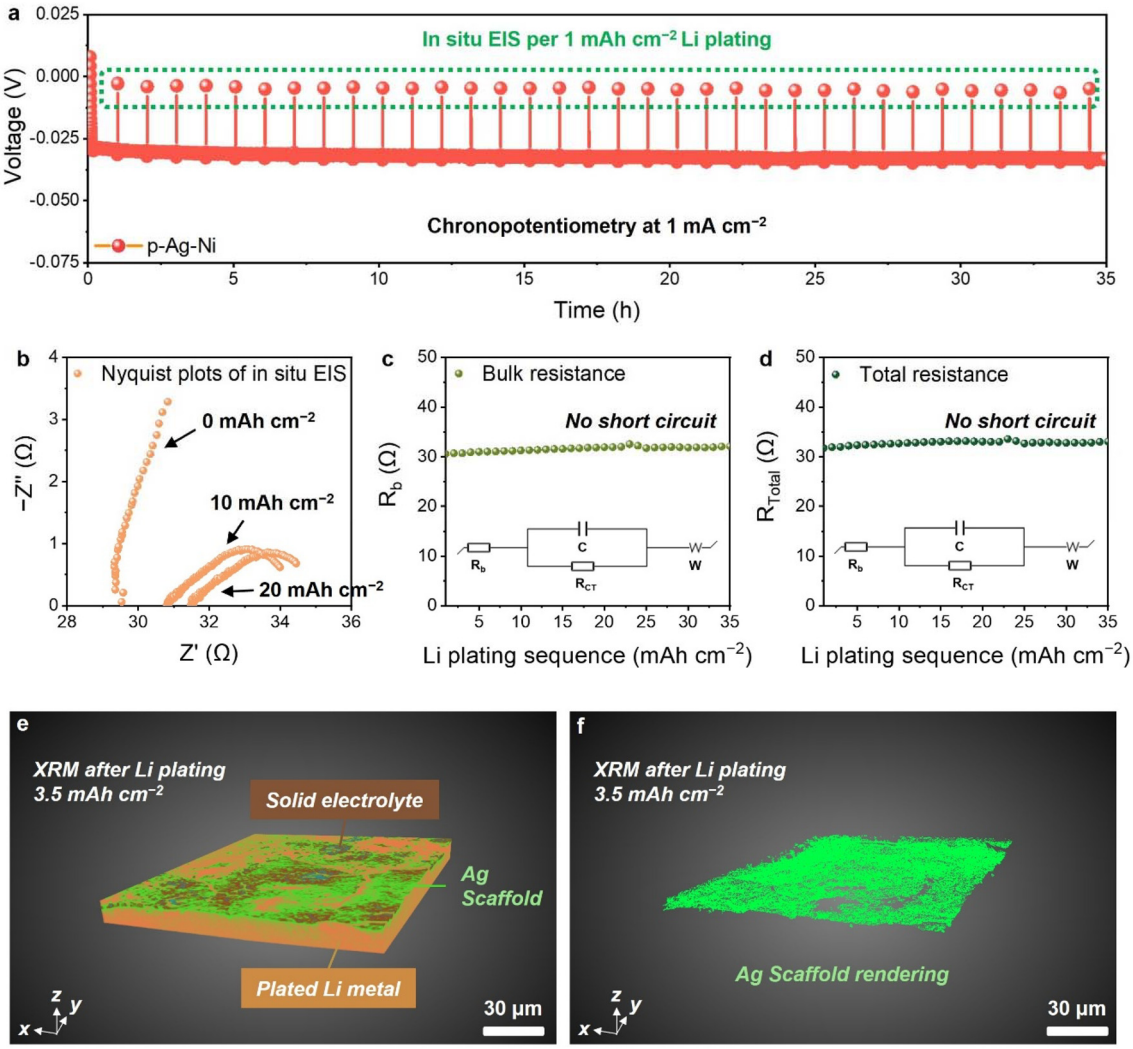

Fig. 4 (a–d) Half-cell chronopotentiometry at a current density of 1 mA cm^{-2} with *in situ* EIS measurements. (a) Voltage–time graph of chronopotentiometry and (b) Nyquist plots recorded during *in situ* EIS. (c and d) Resistance values extracted from fitting (inset: corresponding fitting circuit): (c) bulk resistance (R_b) and (d) total resistance (R_{total}), the sum of R_b and the charge transfer resistance (R_{CT}). (e and f) X-ray microscopy (XRM) 3D color mappings of the (e) p-Ag–Ni layer and (f) residual Ag scaffold after Li plating of 3.5 mAh cm^{-2}. Color code: green (Ag), brown (SE), and orange (Li).

plot, and the total resistance (R_{total}), which combines R_b with the charge transfer resistance (R_{CT}) from the semicircle,[56] both remained stable throughout the Li plating process, even as Li was deposited up to a capacity of 35 mAh cm^{-2}. Cross-sectional SEM-EDS of the cell pellet after 35 mAh cm^{-2} Li deposition revealed a structurally stable configuration (Fig. S9, SI). Ag EDS signals appeared within the SE pellet region—attributable to rapid Ag diffusion into Li—but did not reach the opposite side, indicating that Li did not penetrate the entire pellet and instead deposited stably on the scaffold. This stability demonstrates that the scaffold effectively maintained both the interfacial and overall cell integrity while accommodating such high Li capacities, confirming the ability of the p-Ag–Ni layer to function as a stable, high-capacity scaffold.

X-ray microscopy (XRM) was employed to elucidate the 3D architecture of the scaffold. This advanced technique facilitates comprehensive spatial analysis through tomographic reconstruction, wherein the sample undergoes continuous rotation under sustained X-ray irradiation to generate volumetric datasets. Initial analysis of the pristine p-Ag–Ni electrode demonstrated that the porous Ag overlayer could be readily differentiated through inherent contrast disparities (Fig. S10 and S11, SI), as the Ag component exhibited characteristically enhanced brightness due to its high X-ray attenuation coefficient. To amplify this compositional distinction, false-color mapping was strategically implemented to visualize the intricate porous Ag structural framework (Fig. S12, SI).[57]

XRM was subsequently used to examine the p-Ag–Ni scaffold after electrochemical deposition of 3.5 mAh cm^{-2} Li thereupon (Fig. S13, SI). Tomographic reconstruction revealed preferential Li accumulation within the lower scaffold regions, whereas the uppermost zones were predominantly composed of the original bare Ag matrix. This spatially resolved distribution became markedly more pronounced upon implemen-

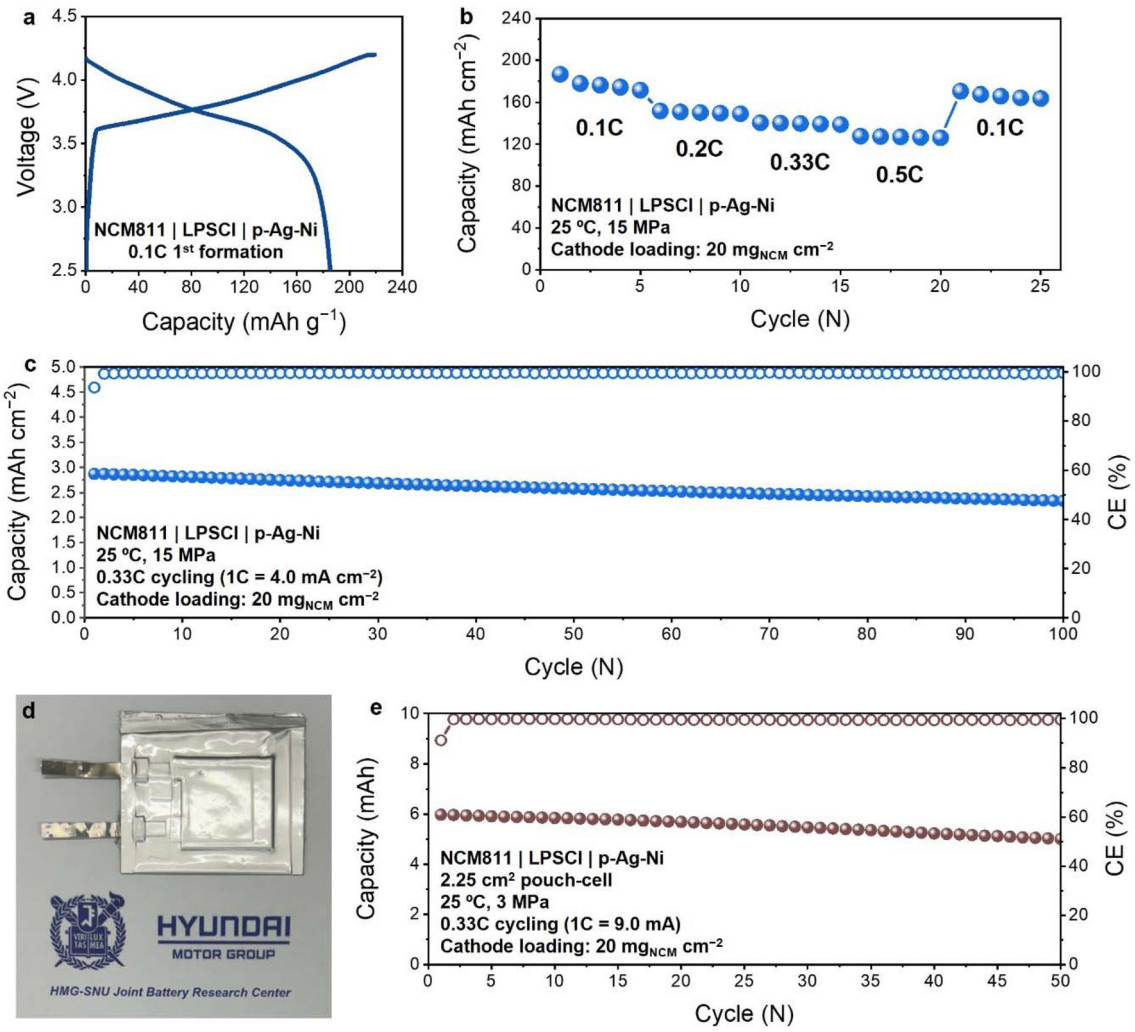

Fig. 5 High-loading full-cell evaluation paired with NCM811 cathode. (a) Voltage profile of the first 0.1C formation cycle. (b) Rate capability test with varying charge and discharge current densities. (c) Cycling performance at a current density of 0.33C. (d and e) Pouch-cell evaluation under low stack pressure of 3 MPa. (d) Photograph of the pouch-cell and (e) cycling performance of the corresponding pouch-cell. Cathode loading: 20 mg$_{NCM}$ cm^{-2}.

tation of contrast-enhanced false-color mapping (Fig. 4e and f). These findings substantiate that the engineered p-Ag–Ni scaffold architecture possesses adequate structural accommodation capacity for elevated areal loadings.

Post-cycling analysis was conducted following 100 successive Li plating–stripping cycles, with the p-Ag–Ni scaffold subjected to comprehensive XRM evaluation (Fig. S14 and S15, SI). The tomographic analysis unveiled partial pore obstruction within the Ag layer relative to the pristine configuration, which was attributed to residual Li deposits that had accumulated throughout the extended cycling protocol. Notably, however, substantial void spaces and networks of microcracks persisted throughout the upper regions of the scaffold, confirming that sufficient free volume had been retained to sustain reversible Li plating–stripping processes during prolonged operation.

Full-cell evaluations were conducted using the $LiNbO_3$-coated $LiNi_{0.8}Co_{0.1}Mn_{0.1}O_2$ (NCM811) cathode material, with a high cathode loading of 20 mg_{NCM} cm^{-2}, to assess the performance of the p-Ag–Ni scaffold under high-capacity full-cell conditions. The results showed that during the first formation cycle at a current density of 0.1C (1C = 4.0 mA cm^{-2}), the cell exhibited a decent ICE of 84.6% and a reversible capacity of 185 mAh g_{NCM}^{-1} (Fig. 5a). The rate performance was subsequently tested by increasing the charge/discharge current densities from 0.1C to 0.5C (Fig. 5b). At 0.5C, the cell retained a high capacity of 128 mAh g_{NCM}^{-1}, and upon returning to 0.1C, the capacity was stably restored to 170 mAh g_{NCM}^{-1}. Due to the high loading of the cathode material, the current density at 0.5C corresponded to 2.0 mA cm^{-2}. Despite this high current density, the p-Ag–Ni anode-less scaffold operated stably without internal short circuits. These results confirmed that the ion-exchange-based porous anode-less material not only ensures high capacity but is also able to withstand high current densities. The prolonged charge–discharge cycling performance was evaluated by applying a current density of 0.33C for both charge and discharge (Fig. 5c and Fig. S16, SI). As a result, the cell retained 81% of its capacity after 100 cycles, thus attesting to stable cycling performance. This marks the successful implementation of a high-capacity ALASSB with an areal capacity of 2.9 mAh cm^{-2}.

Finally, a pouch-cell (Fig. 5d) was fabricated and evaluated under low stack pressure conditions of 3 MPa. ALASSBs typically require high stack pressure (>20 MPa) to ensure stable Li plating/stripping and mechanical integrity, especially for operation at room temperature. Reports of ALASSB systems capable of operating under both low-temperature and low-pressure conditions simultaneously are extremely rare (Table S1, SI).[58,59] In contrast, the p-Ag–Ni scaffold demonstrated successful operation under such mild conditions: the capacity retention was 84% after 50 cycles at 25 °C and 3 MPa, with a high areal capacity of 2.7 mAh cm^{-2} (Fig. 5e and Fig. S17, SI). This performance stems from the scaffold's high surface area—which provides abundant Li nucleation sites—and its porous internal architecture, which accommodates Li within a 3D host framework. Consequently, effective volume expansion is suppressed, enabling stable operation even under low-pressure conditions.

Still, capacity fading remains more rapid under low-pressure than under high-pressure operation. To elucidate the underlying mechanism, we imaged the p-Ag–Ni scaffold after 30 pouch-cell cycles (Fig. S18, SI). The sulfur EDS signal showed that the SE layer retains a distinct interface with Ag—confirming structural stability. However, residual Li persisting on the Ag surface after full discharge implicates dead Li—formed *via* ionic pathway loss likely induced by volume expansion—as a key contributor to capacity fading. Although the porous architecture of p-Ag–Ni effectively suppresses volume expansion, this suppression proves insufficient to fully accommodate the associated volumetric changes, suggesting that incorporating an additional elastic buffer layer will be essential for enabling long-term cycling under low-pressure operation.

Conclusions

In summary, we developed rapid and efficient ion-exchange methodology for synthesizing 3D lithiophilic scaffolds to boost the performance of high-capacity ALASSBs. By immersing a Ni layer in a solution containing Ag^+, we leveraged the difference in the redox potential between the two metals to synthesize Ag nanofibers with a very large surface area through a straightforward process. The resulting p-Ag–Ni scaffold performed exceptionally by enabling stable Li deposition at capacities as high as 35 mAh cm^{-2} without internal short-circuiting. Notably, the ability of the scaffold to maintain stable performance under low stack pressures of 3 MPa highlights its practical viability for real-world applications. The devised ion-exchange strategy presents a versatile and broadly applicable framework for the fabrication of anode-less scaffolds across diverse material systems.

Conflicts of interest

The authors declare no competing interests.

Data availability

The data supporting the findings of this study are available within the article and its supplementary information (SI). Supplementary information is available. See DOI: https://doi.org/10.1039/d6eb00063k.

Acknowledgements

J. W. C. acknowledges support from the National Research Foundation of Korea (NRF) (RS-2024-00335274 and RS-2023-00261543) and the Korea Institute of Machinery and Materials (KIMM) (NK256E). J. W. C. also acknowledges generous support from the Institute of Engineering Research (IOER), the

Institute for Battery Research Innovation (IBRI), the SOFT Foundry Institute, and the Research Institute of Advanced Materials (RIAM) at Seoul National University. This work was also supported by Hyundai Motor Company.

References

1 T. Schmaltz, F. Hartmann, T. Wicke, L. Weymann, C. Neef and J. Janek, *Adv. Energy Mater.*, 2023, **13**, 2301886.
2 J. Janek and W. G. Zeier, *Nat. Energy*, 2023, **8**, 230–240.
3 S. Randau, D. A. Weber, O. Kötz, R. Koerver, P. Braun, A. Weber, E. Ivers-Tiffée, T. Adermann, J. Kulisch, W. G. Zeier, F. H. Richter and J. Janek, *Nat. Energy*, 2020, **5**, 259–270.
4 T. Famprikis, P. Canepa, J. A. Dawson, M. S. Islam and C. Masquelier, *Nat. Mater.*, 2019, **18**, 1278–1291.
5 Y.-K. Sun, *ACS Energy Lett.*, 2020, **5**, 3221–3223.
6 J. Fu, C. Wang, S. Wang, J. W. Reid, J. Liang, J. Luo, J. T. Kim, Y. Zhao, X. Yang, F. Zhao, W. Li, B. Fu, X. Lin, Y. Hu, H. Su, X. Hao, Y. Gao, S. Zhang, Z. Wang, J. Liu, H. Abdolvand, T.-K. Sham, Y. Mo and X. Sun, *Nature*, 2025, **643**, 111–118.
7 A. Manthiram, X. Yu and S. Wang, *Nat. Rev. Mater.*, 2017, **2**, 16103.
8 Q. Zhao, S. Stalin, C.-Z. Zhao and L. A. Archer, *Nat. Rev. Mater.*, 2020, **5**, 229–252.
9 X. Huang, T. Li, W. Fan, R. Xiao and X.-B. Cheng, *Adv. Energy Mater.*, 2024, **14**, 2303850.
10 M. Je, J. Sung, J. Oh, H. Kim, D. Park, H. Kim, Y. Song, S.-M. Lee, J. W. Choi and S. Park, *Chem. Eng. J.*, 2025, **524**, 169406.
11 Y. Kato, S. Hori, T. Saito, K. Suzuki, M. Hirayama, A. Mitsui, M. Yonemura, H. Iba and R. Kanno, *Nat. Energy*, 2016, **1**, 16030.
12 L. Fadillah, L. Braks, J. Oh, M. Liu, H. Türk, D. Tisi, M. Mensi, M. Ceriotti, J. W. Choi and A. Coskun, *Adv. Mater.*, 2026, **38**, e15013.
13 C. Wang, J. T. Kim, C. Wang and X. Sun, *Adv. Mater.*, 2023, **35**, 2209074.
14 S. H. Choi, C. H. Baek, J. Oh, G.-J. Lee, M. Kim, H. Lee, D.-J. Yoo, Y. S. Jung, K. Kim, J.-S. Yu, W. Cho, H. Park and J. W. Choi, *Nat. Commun.*, 2025, **16**, 5871.
15 K. B. Hatzell, X. C. Chen, C. L. Cobb, N. P. Dasgupta, M. B. Dixit, L. E. Marbella, M. T. McDowell, P. P. Mukherjee, A. Verma, V. Viswanathan, A. S. Westover and W. G. Zeier, *ACS Energy Lett.*, 2020, **5**, 922–934.
16 J. Oh, S. H. Choi, H. Kim, W. J. Chung, M. Kim, I. Kim, T. Lee, J. Lee, D. O. Kim, S. Moon, D. Kim and J. W. Choi, *ACS Energy Lett.*, 2025, **10**, 2831–2838.
17 W.-Z. Huang, C.-Z. Zhao, P. Wu, H. Yuan, W.-E. Feng, Z.-Y. Liu, Y. Lu, S. Sun, Z.-H. Fu, J.-K. Hu, S.-J. Yang, J.-Q. Huang and Q. Zhang, *Adv. Energy Mater.*, 2022, **12**, 2201044.
18 S. Y. Han, C. Lee, J. A. Lewis, D. Yeh, Y. Liu, H.-W. Lee and M. T. McDowell, *Joule*, 2021, **5**, 2450–2465.
19 J. A. Lewis, K. A. Cavallaro, Y. Liu and M. T. McDowell, *Joule*, 2022, **6**, 1418–1430.
20 H. Huo and J. Janek, *ACS Energy Lett.*, 2022, **7**, 4005–4016.
21 M. Rana, Y. Rudel, P. Heuer, E. Schlautmann, C. Rosenbach, M. Y. Ali, H. Wiggers, A. Bielefeld and W. G. Zeier, *ACS Energy Lett.*, 2023, **8**, 3196–3203.
22 M. J. Seong, T. Lee, H. C. Ahn, J. Oh, T. Choi, T. Kim, M. Kim, T. Kang, J. Kim, G. Seo and J. W. Choi, *ACS Energy Lett.*, 2025, **10**, 5655–5663.
23 A. Song, W. Zhang, H. Guo, L. Dong, T. Jin, C. Shen and K. Xie, *Adv. Energy Mater.*, 2023, **13**, 2301464.
24 Z. Zhang, X. Zhang, Y. Liu, C. Lan, X. Han, S. Pei, L. Luo, P. Su, Z. Zhang, J. Liu, Z. Gong, C. Li, G. Lin, C. Li, W. Huang, M.-S. Wang and S. Chen, *Nat. Commun.*, 2025, **16**, 1013.
25 T. Lee, M. J. Seong, H. C. Ahn, M. Baek, K. Park, J. Oh, T. Choi and J. W. Choi, *Proc. Natl. Acad. Sci. U. S. A.*, 2025, **122**, e2417053121.
26 J. Kim, I. Jung, K. Lee, I. Hwang, M. Kim, E. Park, D. Park, H. Park, Y. Jeon, G. Park, H. C. Ahn, J. Oh, J. Park, A. Coskun and J. W. Choi, *Adv. Energy Mater.*, 2025, e04147.
27 X. Ji, S. Hou, P. Wang, X. He, N. Piao, J. Chen, X. Fan and C. Wang, *Adv. Mater.*, 2020, **32**, 2002741.
28 X.-B. Cheng, C.-Z. Zhao, Y.-X. Yao, H. Liu and Q. Zhang, *Chem*, 2019, **5**, 74–96.
29 J. Oh, J. L. Frank, R. A. Leising, H. Kim, J. Kim, M. Kim and J. W. Choi, *Energy Environ. Sci.*, 2025, **18**, 7504–7513.
30 H. Wan, Z. Wang, W. Zhang, X. He and C. Wang, *Nature*, 2023, **623**, 739–744.
31 L. Ye and X. Li, *Nature*, 2021, **593**, 218–222.
32 J. Wang and H. Zhu, *ACS Energy Lett.*, 2025, **10**, 2377–2391.
33 C. Heubner, S. Maletti, H. Auer, J. Hüttl, K. Voigt, O. Lohrberg, K. Nikolowski, M. Partsch and A. Michaelis, *Adv. Funct. Mater.*, 2021, **31**, 2106608.
34 S. E. Sandoval, J. A. Lewis, B. S. Vishnugopi, D. L. Nelson, M. M. Schneider, F. J. Q. Cortes, C. M. Matthews, J. Watt, M. Tian, P. Shevchenko, P. P. Mukherjee and M. T. McDowell, *Joule*, 2023, **7**, 2054–2073.
35 N. Lee, J. Oh and J. W. Choi, *Mater. Futures*, 2023, **2**, 013502.
36 J. Oh, J. Kim, S. Bae, H. Kim, T. Lee, S. H. Choi, G. Park, S. Ji, K. J. Kim and J. W. Choi, *Adv. Energy Mater.*, 2025, **15**, e02711.
37 J. Wen, T. Wang, C. Wang, Y. Dai, Z. Song, X. Liu, Q. Yu, X. Zheng, J. Ma, W. Luo and Y. Huang, *Adv. Mater.*, 2024, **36**, 2307732.
38 S. E. Sandoval, C. G. Haslam, B. S. Vishnugopi, D. W. Liao, J. S. Yoon, S. H. Park, Y. Wang, D. Mitlin, K. B. Hatzell, D. J. Siegel, P. P. Mukherjee, N. P. Dasgupta, J. Sakamoto and M. T. McDowell, *Nat. Mater.*, 2025, **24**, 673–681.
39 H. Jo, J.-W. Lee, E. Kwon, S. Yu, B. G. Kim, S. Park, J. Moon, M. J. Ko and H.-D. Lim, *ACS Nano*, 2024, **18**, 35718–35728.
40 X. Zhou, S. Wang, Y. Li, Y. Yang, X. Xiao and G. Chen, *Adv. Energy Mater.*, 2025, **15**, 2403640.
41 J. Oh, T. Lee, N. Lee, Y. Sohn, J. Y. Kim, K. Y. Bae, S. H. Choi and J. W. Choi, *Battery Energy*, 2025, **4**, e70038.

42 J. Oh, H. C. Ahn, H. Kim, T. Lee, I. Kim, M. Je, J. Kim, S. Yang, M. J. Seong, T. Choi, T. Kim, S. H. Choi and J. W. Choi, *Adv. Funct. Mater.*, 2026, **36**, e12023.
43 T. Xie, W. Ye, H. Xiao, B. Wang, Z. Liu, P. Xu, W. Zheng, J. He, H. Zhu, Y. Li, M.-S. Wang and S. Huang, *Chem. Eng. J.*, 2023, **476**, 146609.
44 J. Sun, Y. Cheng, H. Zhang, X. Yan, Z. Sun, W. Ye, W. Li, M. Zhang, H. Gao, J. Han, D.-L. Peng, Y. Yang and M.-S. Wang, *Nano Lett.*, 2022, **22**, 5874–5882.
45 J. Lee, S. H. Choi, G. Im, K.-J. Lee, T. Lee, J. Oh, N. Lee, H. Kim, Y. Kim, S. Lee and J. W. Choi, *Adv. Mater.*, 2022, **34**, 2203580.
46 J. Oh, Y. Sohn and J. W. Choi, *EES Batteries*, 2025, **1**, 566–575.
47 D. Spencer-Jolly, V. Agarwal, C. Doerrer, B. Hu, S. Zhang, D. L. R. Melvin, H. Gao, X. Gao, P. Adamson, O. V. Magdysyuk, P. S. Grant, R. A. House and P. G. Bruce, *Joule*, 2023, **7**, 503–514.
48 F. Liu, T. Cai, Y. Zhu, T. Bai, M. Nie, W. Gan, D. Li, L. Ci and Q. Yuan, *J. Power Sources*, 2025, **647**, 237357.
49 C. Wu, B. Emley, L. Zhao, Y. Liang, Q. Ai, Z. Chen, F. C. R. Hernández, F. Wang, S. Risal, H. Guo, J. Lou, Y. Yao and Z. Fan, *Nano Lett.*, 2023, **23**, 4415–4422.
50 Y.-G. Lee, S. Fujiki, C. Jung, N. Suzuki, N. Yashiro, R. Omoda, D.-S. Ko, T. Shiratsuchi, T. Sugimoto, S. Ryu, J. H. Ku, T. Watanabe, Y. Park, Y. Aihara, D. Im and I. T. Han, *Nat. Energy*, 2020, **5**, 299–308.
51 Y. Sohn, J. Oh, J. Lee, H. Kim, I. Hwang, G. Noh, T. Lee, J. Y. Kim, K. Y. Bae, T. Lee, N. Lee, W. J. Chung and J. W. Choi, *Adv. Mater.*, 2024, **36**, 2407443.
52 X. Li, W. Chen, Q. Qian, H. Huang, Y. Chen, Z. Wang, Q. Chen, J. Yang, J. Li and Y.-W. Mai, *Adv. Energy Mater.*, 2021, **11**, 2000845.
53 L. Wichmann, B. Tengen, P. Yan, P. Lennartz, I. Cekic-Laskovic, M. Winter and G. Brunklaus, *Adv. Funct. Mater.*, 2026, **36**, e11672.
54 W. Huang, Y. Huang, X. Huang, F. Shao, W. Liu and F. Kang, *Small*, 2024, **20**, 2404294.
55 J. Oh, D. Kwon, S. H. Choi, N. Lee, Y. Sohn, T. Lee, T. Lee, J. Y. Kim, K. Y. Bae and J. W. Choi, *Adv. Energy Mater.*, 2025, **15**, 2404817.
56 N. Lee, J. Lee, T. Lee, J. Oh, I. Hwang, G. Seo, H. Kim and J. W. Choi, *ACS Appl. Mater. Interfaces*, 2023, **15**, 34931–34940.
57 J. Oh, S. H. Choi, H. Kim, J. Y. Kim, G.-J. Lee, K. Y. Bae, T. Lee, N. Lee, Y. Sohn, W. J. Chung and J. W. Choi, *Energy Environ. Sci.*, 2024, **17**, 7932–7943.
58 J. Zhang, J. Fu, P. Lu, G. Hu, S. Xia, S. Zhang, Z. Wang, Z. Zhou, W. Yan, W. Xia, C. Wang and X. Sun, *Adv. Mater.*, 2025, **37**, 2413499.
59 J. Oh, W. J. Chung, S. H. Jung, Y. Kim, Y. Lee, Y. J. Nam, S. Lee, C. H. Kim and J. W. Choi, *Energy Storage Mater.*, 2024, **71**, 103606.